Direct observation of Cu, Zn cation disorder in Cu_2ZnSnS_4 (CZTS) solar cell absorber material using aberration corrected scanning transmission electron microscopy

*Budhika G Mendis**[1], *Mervyn D Shannon*[2], *Max CJ Goodman*[1], *Jon D Major*[3], *Richard Claridge*[1], *Douglas P Halliday*[1] *and Ken Durose*[3]

1 Dept of Physics, Durham University, Durham, DH1 3LE, UK
2 SuperSTEM, Daresbury Laboratories, Keckwick Lane, Daresbury, WA4 4AD, UK
3 Stephenson Institute for Renewable Energy, University of Liverpool, Liverpool, L69 7ZF, UK

*Corresponding author. Email: b.g.mendis@durham.ac.uk

Keywords: adamantine compounds; CZTS; donor acceptor pair (DAP) recombination; point defects; solar energy materials.

Chemical analysis of individual atom columns was carried out to determine the crystal structure and local point defect chemistry of Cu_2ZnSnS_4 (CZTS). Direct evidence for a nano-scale composition inhomogeneity, in the form of Zn enrichment and Cu depletion, was obtained. The lateral size of the composition inhomogeneity was estimated to be between ~1.5 and 5 nm. Photoluminescence confirmed the presence of a broad donor-acceptor transition consistent with the observed cation disorder. Areas of relatively high concentration of Zn_{Cu}^{+} anti-site atom donors locally increases the electrostatic potential and gives rise to band bending. Troughs in the conduction band and peaks in the valence band are 'potential wells' for electrons and holes respectively. For a solar cell these prevent minority carrier electrons from diffusing towards the edge of the space charge region, thereby reducing the carrier separation efficiency as well as reducing the carrier collection efficiency of majority carrier holes. Furthermore, electrons and holes 'trapped' within potential wells in close proximity have a high probability of recombining, so that the carrier lifetime is also reduced. High quality CZTS crystals free from composition inhomogeneities are therefore required for achieving high efficiency solar cell devices.

1. Introduction

Cu_2ZnSnS_4 (CZTS) and its mixed selenium counterpart $Cu_2ZnSn(S,Se)_4$ (CZTSSe) are promising absorber layer materials for thin-film solar cells, due to the non-toxicity and abundance of the constituent elements.[1] The record efficiency is currently 10.1% for CZTSSe processed via a hydrazine 'ink'-based approach.[2] The possibility of cheap solution based deposition methods, such as roll-to-roll, ink-jet printing or spin coating,[3] is a further attraction. However, a comparison of a 9.7% efficiency CZTSSe cell with a 13.8% efficient $Cu(In,Ga)Se_2$ (CIGS) cell has shown that the former has a lower open circuit voltage with respect to the band gap and furthermore the minority carrier lifetime is only 1.2 ns compared to 6.2 ns for CIGS.[4] This *suggests* that the crystal quality (e.g. point defects and grain boundaries) has an important effect on CZTS/CZTSSe device efficiency (note that other factors also contribute to measured device efficiencies). Indeed the limited thermodynamic stability of the CZTS phase and loss of Sn during processing makes it difficult to deposit thin-films that are free of secondary phases, such as ZnS, Cu_2SnS_3 etc.[1,5] Experimentally it is found that Cu-poor and Zn-rich thin-films produce the highest efficiency devices,[6] so that a relatively large density of point defects in the form of vacancies and anti-site atoms are to be expected in the off-stoichiometric CZTS compound. Understanding and controlling these

point defects is crucial for improving the crystal quality to a level suitable for photovoltaic applications.

The group III elements in the I-III-VI_2 CIGS chalcopyrite structure can be substituted by Zn (group II) and Sn (group IV) to generate I_2-II-IV-VI_4 CZTS with the kesterite tetragonal crystal structure and space group $I\bar{4}$ (Figure 1a).[7-9] Redistribution of Cu and Zn cations within the (004) planes gives the stannite structure with space group $I\bar{4}2m$ (Figure 1a). Although density functional theory calculations predict kesterite to be the minimum energy structure for CZTS the energy difference between stannite and kesterite is only ~3 meV/atom[9] (Cu and Zn are end-members of the 3d transition metal series so that subtle changes in their distribution between the two phases has only a small effect on the overall crystal energy). This suggests that it is relatively easy to form Cu_{Zn} and Zn_{Cu} anti-site atoms. The point defect formation energy depends on the composition, but theoretical calculations for CZTS under 'Zn-poor' conditions, defined as when the chemical potential of Zn is too low to form any ZnS, has shown that Cu_{Zn} has the lowest formation energy (-0.3 to 0 eV) out of all the point defects.[10] By comparison the formation energy of Zn_{Cu} is above 2 eV, possibly due to the fact that the material is Zn-deficient. Other point defects with relatively low formation energies (i.e. <1 eV) include Cu and Zn vacancies (i.e. V_{Cu} and V_{Zn}), as well as Cu_{Sn} and Zn_{Sn} anti-site atoms.[10] Schorr and co-workers used Rietveld refinement of neutron diffraction data to identify Cu_{Zn} and Zn_{Cu} anti-site atoms in the mixed Cu+Zn (004) planes of CZTS kesterite (Figure 1a).[7,11-12] The point defect density was a function of the thermal history, with samples quenched from the pure element reaction temperature of 750°C showing a higher defect concentration compared to samples cooled slowly at a rate of 1K/hour. Washio *et al*. used synchrotron X-ray diffraction to identify point defects in Cu-poor and Cu-rich CZTS (the anomalous dispersion effect in X-ray scattering was used to distinguish the Cu and Zn atoms).[13] Apart from Cu_{Zn} and Zn_{Cu}, Cu_{Sn} anti-site atoms were also observed, the concentration being higher in the Cu-rich compounds.

Thus far techniques such as photoluminescence, X-ray and neutron diffraction have been used to deduce the presence of point defects in CZTS. These techniques have relatively poor spatial resolution and therefore only provide a volume-averaged result. Aberration corrected scanning transmission electron microscopy (STEM) is explored as a novel method for characterizing the defect chemistry of CZTS at the atomic scale. Figure 1b is a schematic illustration of the technique and shows an electron probe, ~1Å in diameter, focused on a single atom column in an electron transparent specimen (in order to make the electron probe as small as a single atom the spherical aberration in the objective lens must be nulled- hence the term aberration correction[14]). The chemical identity of the atom column is determined by measuring the energy loss of the directly transmitted (i.e. unscattered) electrons, a technique known as electron energy loss spectroscopy (EELS). The characteristic energy loss is due to the electron beam ionizing a core electron from the atom of interest in the solid. An image of the sample is built by rastering the electron probe over the region of interest and at each scan position measuring the electron intensity scattered to high angles via an annular detector. These so-called high angle annular dark field (HAADF) images also contain atomic number information, since atom columns with a higher average atomic number scatter the electron probe more strongly and hence appear brighter in the HAADF image. By tilting the CZTS crystal to the <010> orientation and scanning the electron probe along the [001] *c*-axis it is possible to distinguish between the kesterite and stannite structures. For example in kesterite, the image is a series of atomic columns oriented parallel to the beam i.e. [010] (see arrows in Figure 1a). Reading from the bottom left of the unit cell and moving along the [001] axis, the kesterite sequence is Zn→Cu→Cu, while for stannite it is Cu→Zn→Cu (in the images these sequences are bracketed by two Sn containing columns). The crystal structure may therefore

be identified by EELS chemical analysis of the individual atom columns (the Sn columns are easily identified in the HAADF image since they appear brighter due to the higher atomic number of Sn). The same measurement should also detect anti-site atoms, although since the measurement is taken over an entire atom column and therefore involves several atoms (~88 atoms in a 50 nm thick foil of CZTS), it is unlikely that the sensitivity is high enough to detect a single, isolated anti-site atom, but rather a cluster of anti-site atoms.

In this paper aberration corrected STEM is used to characterize the crystal structure and point defects of CZTS synthesized by solid state reaction of the constituent elements (see section 2 for further details on sample synthesis). The average CZTS composition is $Cu_{1.82}Zn_{0.91}Sn_{1.12}S_{4.15}$, which makes the compound Cu-poor (i.e. Cu/(Sn+Zn) ≈0.9) and Zn-poor (i.e. Zn/Sn ≈0.8). EELS chemical analysis along the [001] direction did not reveal a change in the relative Cu and Zn concentrations between individual atom columns as expected for a pure kesterite or a pure stannite crystal. This could be partly due to mixed Cu, Zn occupancy, as has been observed previously with neutron and X-ray diffraction, but experimental artifacts such as beam spreading could not be ruled out. A large clustering of Zn_{Cu} donor anti-site atoms, best described as a nano-scale composition inhomogeneity, was also observed. The size of the composition inhomogeneity was estimated to be between ~1.5 to 5 nm. Local deviations in the donor or acceptor point defect concentration gives rise to spatially fluctuating electrostatic potentials, which reduce the carrier lifetime, carrier separation and collection efficiencies and hence the overall device efficiency.

2. Experimental Method

CZTS synthesis: CZTS samples were synthesized by solid state reaction of the constituent elements at 800ºC for 24 hours. The purities of the elemental powders, as certified by the manufacturers, were Cu (99.9%), Zn (97.5%), Sn (99.85%) and S (99.5%). Cu, Zn and Sn were placed in a single graphite boat, separate to the S powder which was contained in another graphite boat. Both boats were then sealed in an evacuated quartz ampoule. After heat treatment one end of the ampoule, away from the graphite boats, was first water quenched in order to condense any sulphur vapour which would otherwise form S-rich secondary phases on the sample surface during cooling. Following this procedure the entire ampoule was water quenched. Quenching may retain a higher density of point defects compared to (say) CZTS thin-films synthesized using traditional methods. The starting composition, as determined by weighing the individual elements, was $Cu_{1.5}ZnSnS_4$ but the average composition of the final CZTS material, as determined by energy dispersive X-ray analysis in a scanning electron microscope, was $Cu_{1.82}Zn_{0.91}Sn_{1.12}S_{4.15}$ (the error is expected to be a few atomic%). Small amounts of copper sulphide precipitates were observed at the grain boundaries.

Photoluminescence (PL): A Coherent Innova 70C laser with 457.9 nm lasing wavelength and beam diameter of 1.5 mm was used for the PL experiments. The samples were mounted in a cryostat for cooling to the desired temperature. The luminescence was dispersed by a grating monochromator and collected by a cooled Si photodiode array. A Molelectron laser power meter was used to calibrate the incident laser power.

Transmission Electron Microscopy (TEM): The CZTS samples were crushed and dispersed onto a holey carbon grid for TEM examination. CBED experiments were carried out on a JEOL 2100F FEG TEM operating at 200 kV. Aberration corrected STEM measurements were carried out at the SuperSTEM facility, Daresbury, UK using a Nion UltraSTEM operating at 100 kV. The probe semi-convergence angle was 31 mrad. A Gatan Enfina spectrometer with a 31 mrad semi-collection angle was used for the EELS measurements.

Multislice simulations: The software developed by Kirkland[23] was used for multislice simulations. CZTS lattice parameters of a = 5.7 Å, c = 11.5 Å measured from TEM selected area diffraction patterns, were used for both kesterite and stannite crystal structures. The displacement of sulphur anions from their 'ideal' positions was not taken into account.[7] For CBED patterns (Figure 3c and Figure 3d) the simulation parameters were a 2.9 mrad probe semi-convergence angle (measured directly from the experimental CBED patterns), 1 mm spherical aberration coefficient and -61.3 nm underfocus. The sample thickness was 57 nm and the maximum scattering angle was 279 mrad with a pixel size of 0.03 nm^{-1}. For the pendellösung calculations (Figure 5e) the simulation parameters were a 31 mrad probe semi-convergence angle, zero spherical aberration coefficient and zero defocus. A total of 15 frozen phonon configurations, generated using the Debye-Waller factors listed in [30], were simulated (reference [30] does not contain the Debye-Waller factor for sulphur; hence the Debye-Waller factor for silicon, which has a similar atomic number to sulphur, was substituted).

3. Results and Discussion

Preliminary results from photoluminescence and convergent beam electron diffraction are first presented prior to the main results from aberration corrected STEM.

3.1. Photoluminescence spectroscopy

Figure 2a shows a photoluminescence (PL) spectrum of the CZTS sample acquired at 3 K with a laser power density of 4 Wcm^{-2} at a wavelength of 458 nm. The spectrum is dominated by a broad intense peak at ~1.37 eV with a shoulder at ~1.55 eV (Figure 2a inset) which is close to the band gap of CZTS. Weaker intensity is observed at higher energies and is attributed to secondary phases in the sample. Increasing the laser power causes a blue shift of the 1.37 eV peak (Figure 2b), which suggests that this feature is due to a donor acceptor pair (DAP) transition.[15] DAP transitions have been observed previously in CZTS although the position and width of the peak varies between different samples.[15-17] Hönes *et al*. observed sharp DAP peaks at higher energies (1.47 eV) in CZTS crystals grown using the iodine vapour transport method[18] and attributed the sharpness of the peak to well-defined donor and acceptor energy levels.[16] Romero *et al*. observed the DAP peak to be narrower and at higher energies for CZTS cells with improved efficiencies.[17] The blue shift of the DAP peak was attributed to the predominance of V_{Cu} shallow acceptor defects (over the deeper but lower formation energy Cu_{Zn} defects) in the Cu-poor CZTS samples used for the highest efficiency cells.

The donor and acceptor energy levels were extracted from the temperature dependence of the integrated DAP intensity using Equation (1):[16,19]

$$I(T) = \frac{B}{1 + a_1 \exp\left(-\frac{E_1}{kT}\right) + a_2 \exp\left(-\frac{E_2}{kT}\right)} \quad (1)$$

where $I(T)$ is the integrated DAP intensity at temperature T, a_1, a_2 and B are fitting parameters, k is Boltzmann's constant and E_1, E_2 are the donor and acceptor activation energies. Figure 2c shows $I(T)$ as a function of $(1/T)$ along with the curve of best fit which has the same analytical form as Equation 1. From the best fit curve the donor level was determined to be 13 meV below the conduction band minimum and acceptor level 185 meV

above the valence band maximum. In comparison Hönes *et al*. found a 5 meV donor level and 30 meV acceptor level for a narrow DAP transition at 1.47 eV.[16] Theoretical calculations have shown that out of the low energy defects the V_{Cu} and Cu_{Zn} acceptor levels are at 20 and 120 meV above the valence band maximum respectively while the Zn_{Cu} donor level is 150 meV below the conduction band minimum.[10] The relatively deep acceptor level in our sample (185 meV) suggests that the dominant acceptor defect is not V_{Cu}. Cu_{Zn} could be the dominant deep acceptor defect but the fact that the sample is Cu-poor, as well as Zn-poor, means that there must be other anti-site atoms on the Cu sites, such as for example Sn_{Cu} from the excess Sn in the sample (according to [10] Sn_{Cu} is a mid-gap state and will not therefore contribute to the luminescence intensity due to non-radiative recombination). Other possible candidates include the V_{Zn} deep acceptor level which also has a relatively low formation energy.[10] The donor level in our sample, and that of Hönes *et al*.[16], is shallow (13 meV) and cannot be easily identified. In section 3.3 direct evidence for Zn_{Cu} is presented but this is a relatively deep donor.[10] Since the lower conduction band in CZTS is due to hybridization of Sn-*s* and S-*p* states[9,20] it is tentatively suggested that the shallow donor could involve Sn and/or S atoms. Finally it should be noted that since the DAP peak in our sample is relatively broad (full width at half maximum ~0.2 eV) the donor and acceptor levels extracted by curve fitting are likely to be a weighted average of all the DAP transitions taking place and hence unambiguous identification of the dominant point defects is not straightforward.

3.2. Convergent beam electron diffraction

The kesterite and stannite crystal structures differ in the Cu and Zn cation ordering with the result that the energy difference between the two phases is only 3 meV/atom.[9] Cu^+ and Zn^{2+} have an identical number of electrons per ion (28) so that their X-ray and electron scattering powers are similar. Crystal structure identification has therefore been carried out using Rietveld refinement of either neutron diffraction or synchrotron X-ray diffraction data, the latter being acquired under anomalous dispersion conditions in order to distinguish between Cu^+ and Zn^{2+} ions. These techniques require relatively large volumes of material and hence cannot be readily applied to a CZTS thin-film absorber layer. To overcome this limitation convergent beam electron diffraction (CBED) in a transmission electron microscope is explored here as an alternative technique. CBED contains information on the point group symmetry of the small crystal volume probed by a focused electron beam a few nanometers in size. The point group of kesterite is $\bar{4}$ while that of stannite is $\bar{4}2m$ so that the crystal structure of individual grains in a thin-film can potentially be determined using this technique. However, since the electron scattering powers of Cu^+ and Zn^{2+} are similar a thick sample is required to induce dynamic electron diffraction; this is however typically the case when determining point groups using CBED. For more details on CBED and point group determination see for example [21-22].

Table 1 summarises the expected symmetry of CBED patterns for kesterite and stannite structures in the <100> and <110> orientations.[22] Symmetry of the unscattered 000 disc (bright field symmetry) and of the whole-pattern is specified. Furthermore two symmetry forms are identified, namely ‘full’ and ‘projection’ symmetry where scattering from the higher order Laue zones are strong and weak respectively. Projection symmetry corresponds to the case where 3D scattering from the entire crystal is weak so that the observed symmetry corresponds to a 2D projection of the crystal along the electron beam direction. Experimental CBED patterns for CZTS acquired along <100> and <110> directions only displayed projection symmetry (i.e. no higher order Laue zone rings or lines were observed). Table 1 indicates that under these conditions the two crystal structures can be distinguished from CBED patterns acquired along <100>, but not along <110>. Figure 3a shows the selected area

electron diffraction pattern of CZTS in the [010] orientation and Figure 3b is the corresponding CBED pattern showing bright field and whole-pattern 2*mm* symmetry consistent with the stannite structure (Table 1). CBED patterns for the kesterite and stannite structures were simulated using the multislice method[23] and the results for a 57 nm thick specimen are shown in Figure 3c and Figure 3d respectively. The overall agreement with the experimental result is good. The simulated results for kesterite (point group $\bar{4}$) and stannite (point group $\bar{4}2m$) are *visually* similar and display 2*mm* bright field and whole-pattern symmetry for the higher symmetry crystal structure stannite (it should be noted that the displacement of sulphur anions from their 'ideal' positions[7] were not included in the simulations, but this is not expected to make a significant difference since scattering from the low atomic number sulphur ions is relatively weak). This can be explained by assuming that scattering from Cu and Zn cations is largely indistinguishable, so that the CBED patterns correspond to that of a crystal with point group $\bar{4}2m$. However, a more detailed quantitative analysis of the intensity levels in the simulated CBED patterns did reveal the expected *m* whole-pattern symmetry for kesterite (Figure 3c) and 2*mm* whole-pattern symmetry for stannite (Figure 3d) although the intensity differences are small and unlikely to be detected in a real experiment where the contrast is a lot poorer. Simulations for much thicker specimens (i.e. 200 nm) produced similar results for the two structures despite the enhanced dynamic electron diffraction in the thick crystal. Our attempt to characterize CZTS crystal structure using the CBED method is therefore unsuccessful.

3.3. Aberration corrected scanning transmission electron microscopy

Figure 4 is a HAADF image of the CZTS sample in the [010] orientation acquired using an aberration corrected STEM. The bright atom columns in the image correspond to Sn and have a periodic, centered rectangular arrangement that is consistent with the kesterite and stannite structures (Figure 1a). Apart from kesterite and stannite I_2-II-IV-VI_4 compounds can also have a primitive-mixed CuAu (PMCA) structure (space group $P\bar{4}2m$; Figure 1a) which is derived from the CuAu-like I-III-VI_2 ternary compound.[8,9] PMCA can easily be distinguished from kesterite and stannite since the Sn atom columns form a primitive rectangular net when viewed in the [010] projection. This is however not observed in Figure 4 and is consistent with the theoretical prediction that PMCA is the higher energy structure, although in CZTS the energy is only slightly greater (by 0.3 eV) than stannite.[9]

In Figure 5a EELS spectra are acquired along the arrowed line which is parallel to the [001] *c*-axis. The arrow indicates the scan direction of the electron probe during EELS acquisition. A data set which contains EELS spectra at each scan point of the electron beam is known as a 'spectrum image'.[24] The atom columns of interest are the three atom columns, atom1, atom2 and atom3, positioned between the two bright Sn columns labeled Sn1 and Sn2 respectively. As described in section 1 chemical analysis of these three atom columns is sufficient to distinguish between pure kesterite and pure stannite crystal structures. Figure 5b shows the HAADF intensity profile acquired simultaneously with the EELS signal at each analysis position. The atom columns of interest are easily identified in Figure 5b so that the composition of a given atom column can be determined by integrating the EELS spectra from the corresponding pixels in the spectrum image. The EELS spectrum for the atom column labeled atom2, extracted in the above manner, is shown in Figure 5c. The energy loss region of the EELS spectrum contains the Cu and Zn L-edges (the L-edge is due to ionization of a 2*p* core electron) at energy loses of ~931 eV and ~1020 eV respectively. Hence there is some overlap between the two L-edges. A ~20 eV energy window was selected prior to the energy threshold of the Zn L-edge and the intensity within that window modeled using a power law function.[25] Extrapolation of the power law function to higher energy losses and subtraction

removes (approximately) the contribution from the Cu L-edge, with the residual intensity being due to the Zn L-edge. The power law background and the residual Zn L-edge intensity are both superimposed in Figure 5c.

Figure 5d shows the EELS spectra for atom columns atom1, atom2, atom3 and Sn1. The EELS spectra for atom1, atom2 and atom3 have similar shape and intensity values (in Figure 5d the atom2 and atom3 spectra have been vertically shifted for clarity) and hence similar concentrations of Cu and Zn as well. This does not agree with the expected trend for a pure kesterite or pure stannite phase, which could suggest the presence of Cu and Zn cation disorder along the atom columns. The presence of Cu_{Zn} and Zn_{Cu} anti-site atoms is not unexpected as it has been previously observed in neutron and X-ray diffraction.[7,11-13] However, in the present case care must be taken that the measured EELS spectra represent the true composition of the atom column of interest and are free of experimental artifacts such as beam spreading. Although the electron probe at the entrance surface of the specimen is as small as a single atom column the electron probe will channel along the atom column for only a finite distance before dechanneling causes the beam to spread to neighbouring atom columns.[26-27] The EELS spectrum measured from a 'thick' crystal will therefore contain the contribution from the atom column of interest superimposed on a more or less uniform background due to neighbouring atom columns. Some indication of the magnitude of the background contribution can be obtained by examining the EELS spectrum measured for the Sn1 atom column, as it should not contain any intensity from Cu and Zn-L edges if it is a pure Sn column. This is not a perfect comparison as dechanneling will be relatively stronger in the higher atomic number Sn column and because the increase in high angle scattering gives rise to a smaller intensity in the unscattered beam passing through the EELS spectrometer entrance aperture. The EELS spectrum for Sn1 has the same shape as that of atom1 but slightly lower intensity. This indicates that the measured EELS spectra are dominated by the background contribution. As a more quantitative analysis of beam spreading the electron probe pendellösung (i.e. electron beam intensity vs. depth) was simulated using the frozen phonon multislice method.[23] Simulations were carried out for a probe incident on a Zn column and on a Sn column in a pure kesterite crystal, the results of which are shown in Figure 5e. The probe pendellösung shows an oscillatory behaviour due to part of the intensity being transferred back and forth between neighbouring atomic columns. For the probe incident on the Zn column the first intensity minimum is at ~5 nm and by 30 nm the probe intensity on the Zn column has decreased to ~12% of its value at the entrance surface. Dechanneling of the probe focused on the Sn column is even greater due to the higher atomic number of Sn. The thickness of our specimen is assumed to be several tens of nanometers due to the fact that the measurements were carried out away from the specimen edge, where the thickness is least, in order to avoid electron beam damage. Therefore under the given experimental conditions no meaningful conclusion can be made about Cu, Zn cation disorder due to beam spreading artifacts in the EELS measurements.

Figure 6a shows a separate region of the CZTS crystal from which EELS analysis was carried out. The atom columns have been labeled in a manner consistent with the previous example. Figure 6b is the HAADF intensity profile acquired simultaneously with the EELS measurements and in Figure 6c the extracted EELS spectra for atom1, atom2 and atom3 are displayed (the spectra for atom2 and atom3 are vertically shifted for clarity). The EELS spectra have similar shape and intensity for all three atom columns. However, the atom columns are Zn-rich and are virtually depleted of any Cu, indicating a high concentration of Zn_{Cu} anti-site atoms. This is in contrast to the previous example (i.e. mixed Cu, Zn atom columns) which was reproduced in several other measurements as well. The EELS signal extracted for Sn1 was virtually identical to that for atom1 (results now shown), indicating that

the background contribution to the measurement is relatively large. It is possible to obtain an upper estimate for the beam broadening based on geometric spreading of a convergent probe. The electron probe has a semi-convergence angle of 31 mrad so that for a 50 nm thick specimen beam spreading takes place over a 1.5 nm radius (this is approximately three times the *a*-lattice parameter of a CZTS unit cell). Figure 6d shows the average EELS spectrum acquired over a 10x10 nm area that also contains the atom columns analysed in Figure 6a (the electron probe was rapidly scanned over the area of interest during prolonged collection, i.e. 30 s, of the EELS spectrum). Compared to Figure 6b there is considerably more Cu over the scanned area, with the Cu/Zn atom ratio being 0.4 ± 0.1 (Hatree-Slater partial cross-sections were used to estimate the ionization probability).[25] Hence the Zn_{Cu} anti-site atoms observed in Figure 6c has the form of a nano-scale composition inhomogeneity, with the lateral (i.e. perpendicular to the beam) dimension being between ~1.5 nm and 5 nm (i.e. half the scanned area dimension).

The excess Zn_{Cu} anti-site atoms, due to the composition inhomogeneity, form a region of uncompensated donor ions that are positively charged. The higher electrostatic potential causes a local decrease in the conduction and valence band energies. The electronic band structure for CZTS is therefore not flat, but contains peaks and troughs due to a spatially fluctuating electrostatic potential that follows the profile of the composition inhomogeneities in the sample (Figure 7; a peak in the conduction and valence band energies is caused by uncompensated acceptor ions that are negatively charged). This has important consequences for CZTS as an absorber layer material in solar cell devices. For example, photo-excited electrons (holes) are likely to become 'trapped' within the conduction (valence) band trough (peak) and require thermal energy to escape. The effectiveness of a particular 'potential well' depends on the degree of band bending and hence electrostatic potential due to the composition inhomogeneity. In the case of Figure 6c the atom columns are virtually depleted of any copper (in a 50 nm thick specimen each atom column will contain ~88 atoms) so that the high concentration of Zn_{Cu}^{+} donors induces a large electrostatic potential. For solar cells the presence of deep potential wells reduces the probability that minority carriers (electrons in the case of *p*-type CZTS) can diffuse towards the edge of the space charge region and hence the carrier separation efficiency is reduced. This is consistent with the observation that the external quantum efficiency in CZTS increases in reverse bias mode (compared to zero bias) due to the space charge region becoming wider.[1,4] Holes, injected from the *n*-type semiconductor (e.g. CdS in a typical CZTS device [1]) and photo-generated within the CZTS absorber layer, can also become 'trapped' at potential wells, thereby reducing the carrier collection efficiency. The probability of recombination is also significantly enhanced if a 'trapped' electron and 'trapped' hole are sufficiently close to one another such that their wavefunctions overlap. In Figure 6c the lateral size of the Zn enrichment was estimated to be between ~1.5 and 5 nm. The size of Wannier-Mott excitons in inorganic semiconductors is typically a few nanometers[28] and is not significantly different to the size of the composition inhomogeneity, which suggests that recombination of electrons and holes, 'trapped' within neighbouring potential wells, should be particularly dominant in CZTS. The fact that the minority carrier lifetime in CZTS is only 1.2-3.1 ns compared to 6.2 ns for CIGS[2,4] or 20 ns for CdTe[29] supports this conclusion.

Finally it should be pointed out that the spatially fluctuating electrostatic potential is believed to be the origin of the broad DAP peak observed in PL experiments (Figure 7).[16] However our results suggest that there is potentially a second reason for peak broadening, that of degenerate doping of the CZTS material. If the concentration of donors (acceptors) is large, i.e. of the order of the conduction (valence) band effective density of states, interaction between neighbouring donors (acceptors) causes broadening of the donor (acceptor) energy

level into a continuous band. In the Zn-rich composition, the inhomogeneity observed in Figure 6 is sufficiently high that the material is virtually depleted of Cu. From the crystal structure of CZTS it may be estimated that the Zn_{Cu}^{+} anti-site donor concentration is therefore ~10^{22} cm^{-3} (assuming that all Cu-sites are filled with Zn leaving no vacancies), which is several orders of magnitude larger than the conduction band effective density of states for a typical inorganic semiconductor (i.e. 10^{17}-10^{19} cm^{-3}) [31]. The CZTS material is therefore degenerately doped within the composition inhomogeneity, so that DAP transitions within this region can take place over a range of energies. The width of the DAP peak could therefore be used as a qualitative measure of the chemical homogeneity of CZTS, especially in thin-film form, with highly uniform material displaying a narrow DAP peak. However, more work correlating DAP peak width with composition inhomogeneities is required to confirm this.

4. Conclusions

Aberration corrected STEM was used to measure the compositions of Cu/Zn atom columns along the [001] *c*-axis in [010]-orientated CZTS crystals. The majority of atom columns showed mixed Cu, Zn occupancy. While this could be due to genuine cation disorder experimental artifacts, in the form of beam spreading, could not be ruled out. A nano-scale composition inhomogeneity, where the atom columns are Zn-rich and contain virtually no Cu, was also observed. The lateral size of the inhomogeneity was estimated to be between ~1.5 and 5 nm. The high concentration of Zn_{Cu}^{+} donors creates a region of high electrostatic potential that leads to band bending. The band structure for CZTS is therefore not flat but contains peaks and troughs in the conduction and valence bands that follow the spatial profile of the composition fluctuations. These act as potential wells for electrons and holes so that the carrier lifetime, carrier separation and carrier collection efficiencies are reduced. CZTS crystals of high quality are therefore necessary for realising high efficiency solar cell devices. The composition inhomogeneities also lead to broadening of the DAP peak in PL spectroscopy, so that the DAP peak width could potentially be used as a qualitative measure of the chemical uniformity, especially in thin-film CZTS. It is worth mentioning that CZTS is typically reported to be *p*-type and the composition inhomogeneity observed in this paper is *n*-type so that it is unlikely to be the dominant point defect. PL data also points to the dominant donor being a shallow defect (i.e. 13 meV below the conduction band minimum) rather than Zn_{Cu}^{+} anti-site atoms. The results demonstrate that CZTS is disordered on a nano-scale and that techniques such as photoluminescence and aberration-corrected STEM combined with more 'bulk volume' measurements, such as neutron diffraction, are required to fully characterize the material. Finally attempts to use CBED to characterize the crystal structure of CZTS at the nano-scale were unsuccessful, due to electron scattering from Cu and Zn cations being indistinguishable, even in the limit of dynamic diffraction.

Acknowledgements

Financial support from EPSRC is gratefully acknowledged, in particular EP/1028781 (Budhika Mendis), the RCUK energy programme, Supergen PV21 (EP/F029624/1; Ken Durose) and the EPSRC UK National Facility for Aberration-Corrected STEM at SuperSTEM.

References

[1] D. B. Mitzi, O Gunawan, T. K. Todorov, K. Wang, S. Guha, *Sol. Energy Mater. Sol. Cells* **2011**, *95*, 1421-1436.
[2] D.A.R. Barkhouse, O. Gunawan, T. Gokmen, T. K. Todorov, D.B. Mitzi, *Prog. Photovolt: Res. Appl.* **2012**, *20*, 6-11.
[3] W. Ki, H. W. Hillhouse, *Adv. Energy Mater.* **2011**, *1*, 732-735.
[4] O. Gunawan, T. K. Todorov, D. B. Mitzi, *Appl. Phys. Lett.* **2010**, *97*, 233506 (3 pages).
[5] I. D. Olekseyuk, I. V. Dudchak, L. V. Piskach, *J. Alloys Compds.* **2004**, *368*, 135-143.
[6] H. Katagiri, K. Jimbo, M. Tahara, H. Araki. K. Oishi, *Mater. Res. Soc. Symp. Proc.* **2009**, *1165*, M04-01.
[7] S. Schorr, *Thin Solid Films* **2007**, *515*, 5985-5991.
[8] S. Chen, X. G. Gong, A. Walsh, S. -H. Wei, *Phys. Rev. B* **2009**, *79*, 165211 (10 pages).
[9] S. Chen, X. G. Gong, A. Walsh, S. -H. Wei, *Appl. Phys. Lett* **2009**, *94*, 041903 (3 pages).
[10] S. Chen, J. –H. Yang, X. G. Gong, A. Walsh, S. –H. Wei, *Phys. Rev. B* **2010**, *81*, 245204 (10 pages).
[11] S. Schorr, H. –J. Hoebler, M. Tovar, *Eur. J. Mineral.* **2007**, *19*, 65-73.
[12] S. Schorr, *Sol. Energy Mater. Sol. Cells* **2011**, *95*, 1482-1488.
[13] T. Washio, H. Nozaki, T. Fukano, T. Motohiro, K. Jimbo, H. Katagiri, *J. Appl. Phys.* **2011**, *110*, 074511 (4 pages).
[14] O. L. Krivanek, G. J. Corbin, N. Dellby, B. F. Elston, R. J. Keyse, M. F. Murfitt, C. S. Own, Z. S. Szilagyi, J. W. Woodruff, *Ultramicroscopy* **2008**, *108*, 179-195.
[15] K. Tanaka, Y. Miyamoto, H. Uchiki, K. Nakazawa, H. Araki, *Phys. Stat. Sol.(a)* **2006**, *203*, 2891-2896.
[16] K. Hönes, E. Zscherpel, J. Scragg, S. Siebentritt, *Physica B* **2009**, *404*, 4949-4952.
[17] M. J. Romero, H. Du, G. Teeter, Y. Yan, M. M. Al-Jassim, *Phys. Rev. B* **2011**, *84*, 165324 (5 pages).
[18] R. Nitsche, D. F. Sargent, P. Wild, *J. Cryst. Growth* **1967**, *1*, 52-53.
[19] J. Krustok, H. Collan, K. Hjelt, *J. Appl. Phys.* **1997**, *81*, 1442-1445.
[20] C. Persson, *J. Appl. Phys.* **2010**, *107*, 053710 (8 pages).
[21] J. C. H. Spence, J. M. Zuo, *Coherent Microdiffraction*, Plenum Press, New York, USA **1992**.
[22] B. F. Buxton, J. A. Eades, J. W. Steeds, G. M. Rackham, *Phil. Trans. Roy. Soc.* **1976**, *281*, 171-194.
[23] E. J. Kirkland, *Advanced Computing in Electron Microscopy*, Plenum Press, New York, USA **1998**.
[24] C. Jeanguillame, C. Colliex, *Ultramicroscopy* **1989**, *28*, 252-257.
[25] R. F. Egerton, *Electron Energy-Loss Spectroscopy in the Electron Microscope*, Plenum Press, New York, USA **1996**.
[26] Y. Peng, P. D. Nellist, S. J. Pennycook, *J. Electron Microsc.* **2004**, *53*, 257-266.
[27] B. G. Mendis, *Acta Cryst. A* **2010**, *66*, 407-420.
[28] M. Fox, *Optical Properties of Solids*, Oxford University Press, Oxford, UK **2001**.
[29] D. R. Wright, D. Bradley, G. Williams, M. Astles, S. J. C. Irvine, C. A. Jones, *J. Cryst. Growth* **1982**, *59*, 323-331.
[30] H. X. Gao, L. M. Peng, *Acta Cryst. A* **1999**, *55*, 926-932.
[31] D. Neaman, *An introduction to semiconductor devices*, McGraw-Hill, New York, USA **2006**.

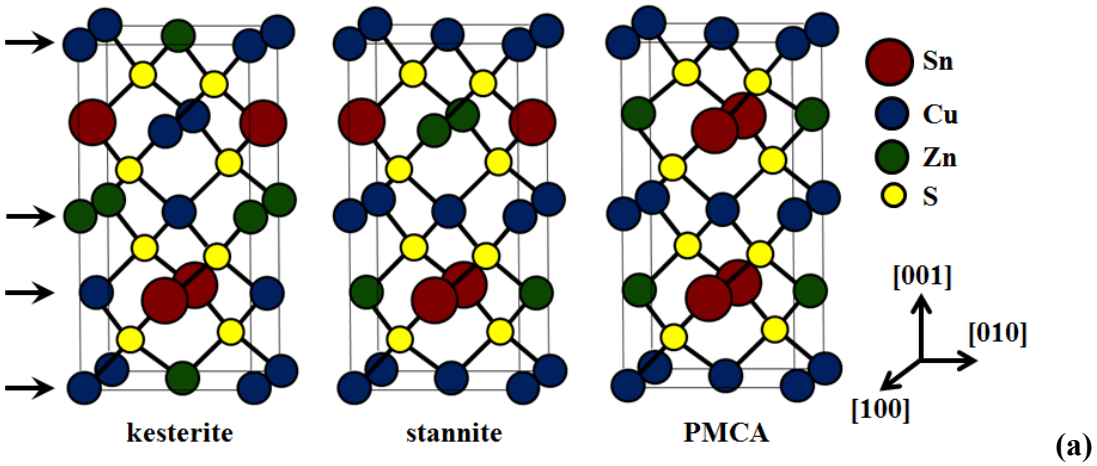

(a)

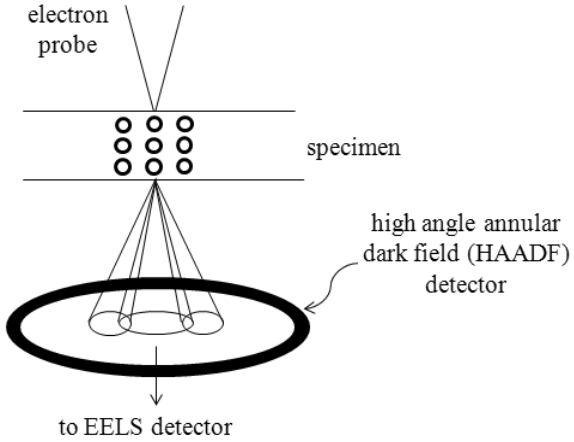

(b)

Figure 1. a) Kesterite, stannite and primitive mixed CuAu (PMCA) tetragonal crystal structures of CZTS. Kesterite and stannite differ in the ordering of Cu and Zn cations within the (004) planes. b) Schematic of the experimental set up used in aberration corrected STEM.

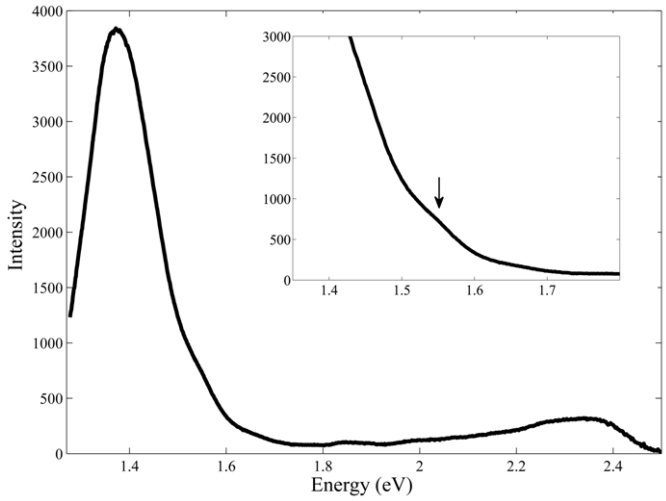

(a)

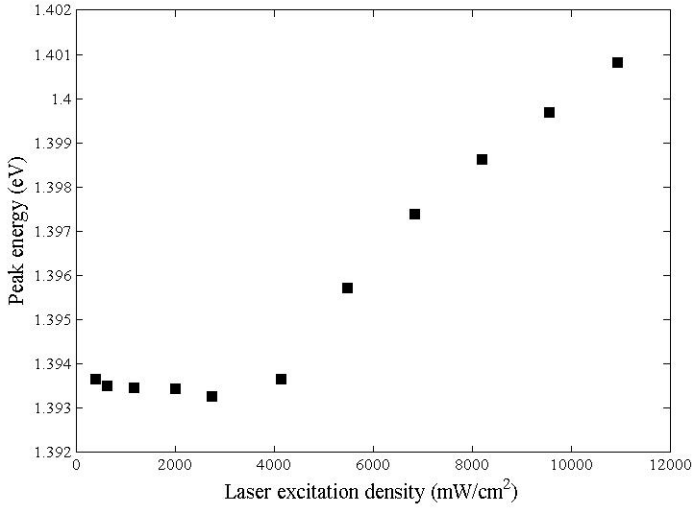

(b)

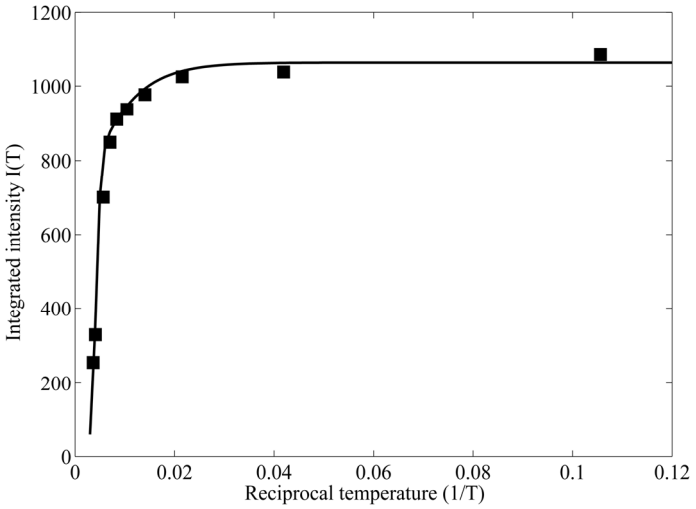

(c)

Figure 2. a) Photoluminescence spectrum of CZTS at 3 K acquired using a 4 Wcm^{-2} laser power density. The broad intense peak at ~1.37 eV is a donor acceptor pair (DAP) transition. A weak shoulder at ~1.55 eV is also observed (figure inset). Higher energy peaks are due to secondary phases in the bulk sample. b) Change in the DAP peak energy as a function of the laser excitation density. c) Integrated intensity $I(T)$ of the DAP peak plotted as a function of the reciprocal temperature ($1/T$). The solid line is the best fit curve to the experimental data modeled using Equation 1. The laser power density is 4 Wcm^{-2}.

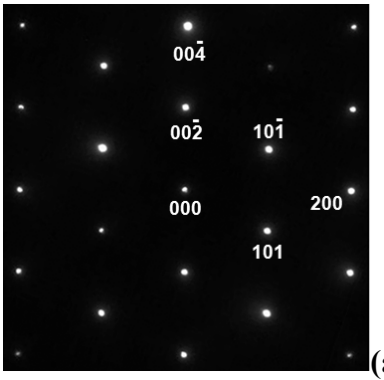

(a)

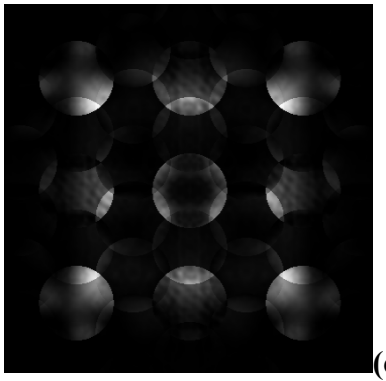

(c)

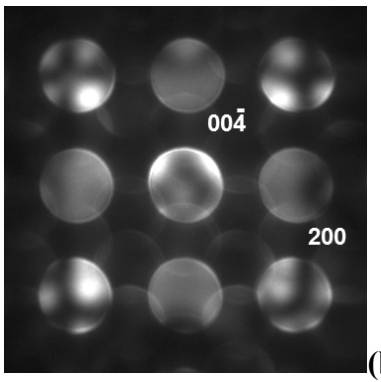

(b)

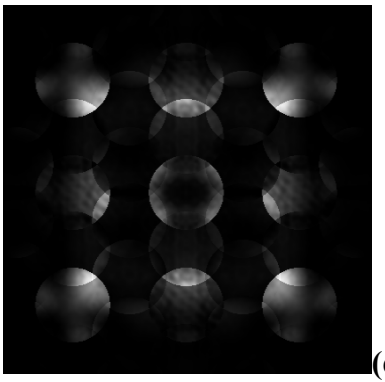
(d)

Figure 3. a) Selected area electron diffraction pattern of a CZTS crystal in the [010] orientation and b) the corresponding [010] convergent beam electron diffraction (CBED) pattern. Multislice simulated CBED results for pure kesterite and pure stannite crystals are shown in c) and d) respectively. The specimen thickness in the simulation was 57 nm.

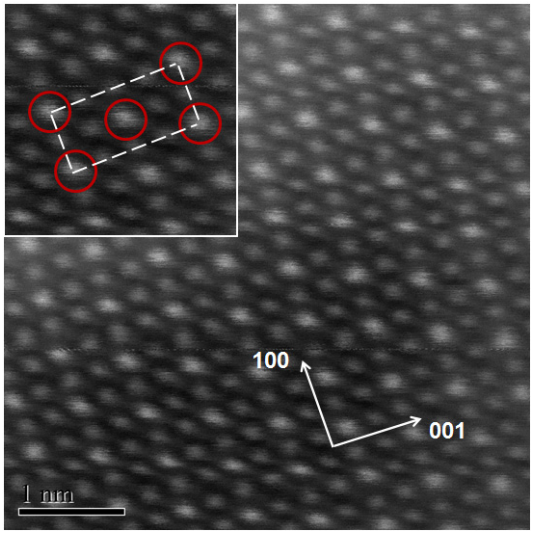

Figure 4. High angle annular dark field (HAADF) image of [010]-oriented CZTS acquired using aberration corrected STEM. The bright atom columns correspond to Sn and have a centred rectangular arrangement (figure inset). The waviness of the atom planes is due to STEM scan distortions.

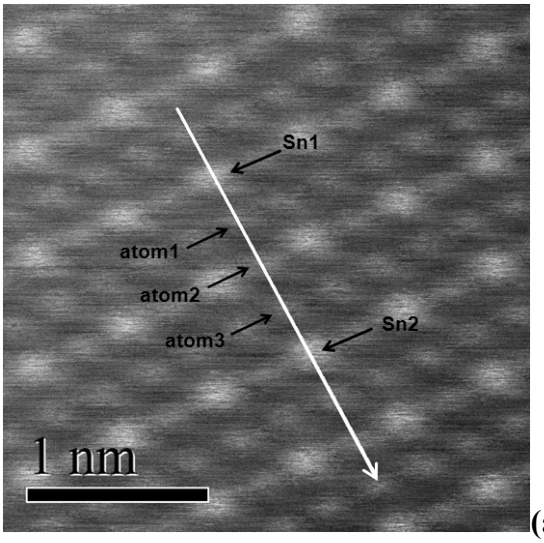

(a)

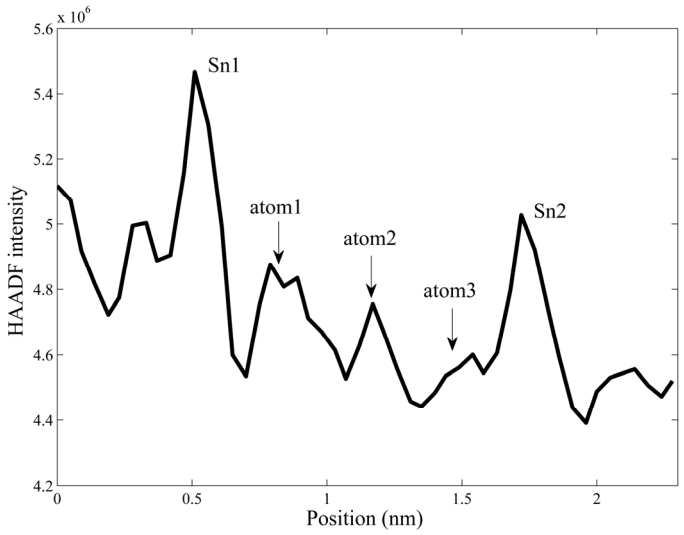
x 10^6
HAADF intensity
Position (nm)
Sn1
atom1
atom2
atom3
Sn2

(b)

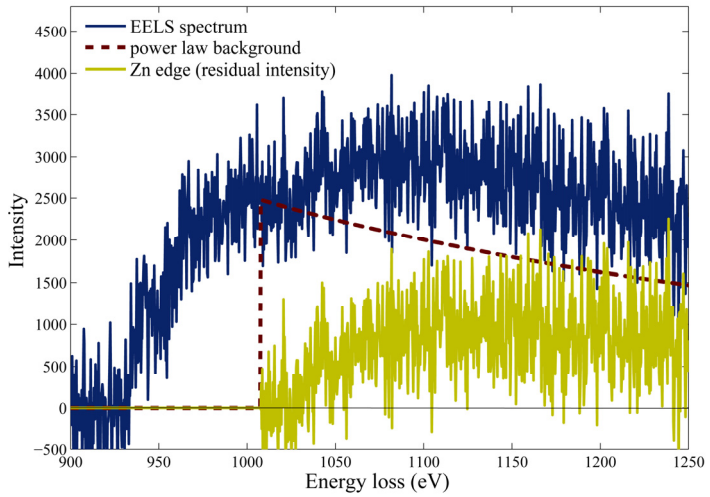
EELS spectrum
power law background
Zn edge (residual intensity)
Intensity
Energy loss (eV)

(c)

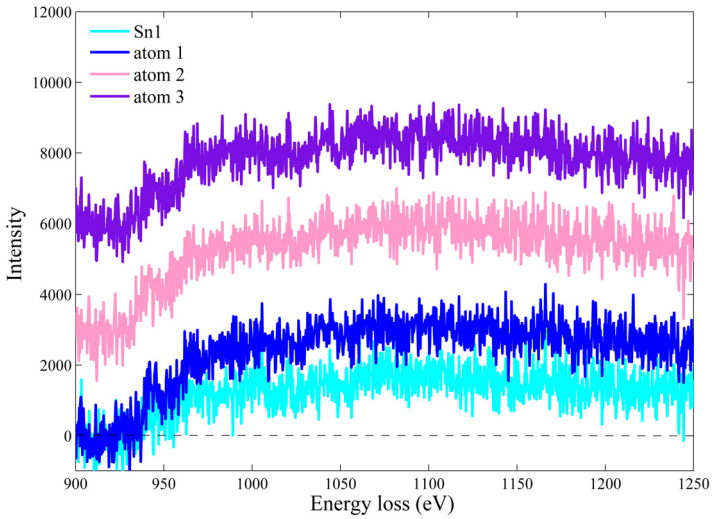
Sn1
atom 1
atom 2
atom 3
Intensity
Energy loss (eV)

(d)

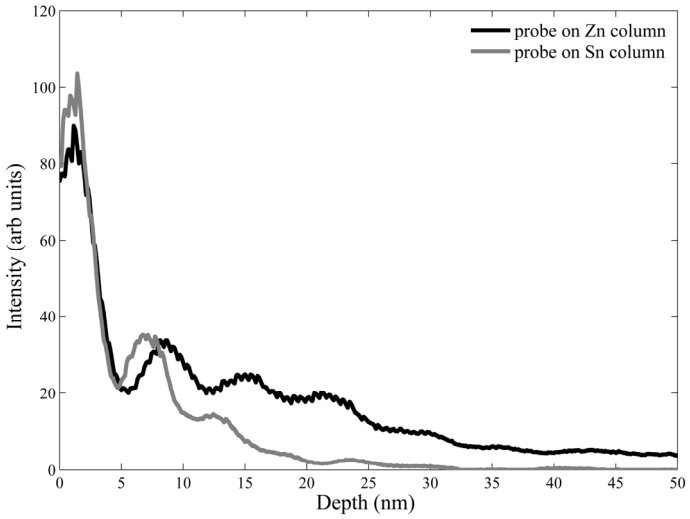

(e)

Figure 5. a) HAADF image of [010]-oriented CZTS. The arrow indicates the direction and line over which EELS spectra are acquired. The atom columns of interest are labeled Sn1, atom1, atom2, atom3 and Sn2 with the first and last being Sn atom columns. b) HAADF intensity profile acquired simultaneously during EELS measurement. c) Extracted EELS spectrum for the atom column labeled atom2. The EELS spectrum consists of Cu and Zn L-edges which are partly overlapping. To extract the higher energy loss Zn L-edge a power law is fitted within a ~20 eV window positioned just before the energy threshold of Zn-L and extrapolated to higher energy losses. The residual, obtained by subtracting the power law background from the EELS spectrum, gives the Zn L-edge. d) Extracted EELS spectra for atom columns Sn1, atom1, atom2 and atom3 with the last two spectra vertically shifted for clarity. e) Frozen phonon multislice simulated pendellösung plots for a STEM probe incident on Zn and Sn atom columns respectively in a [010]-oriented pure kesterite crystal.

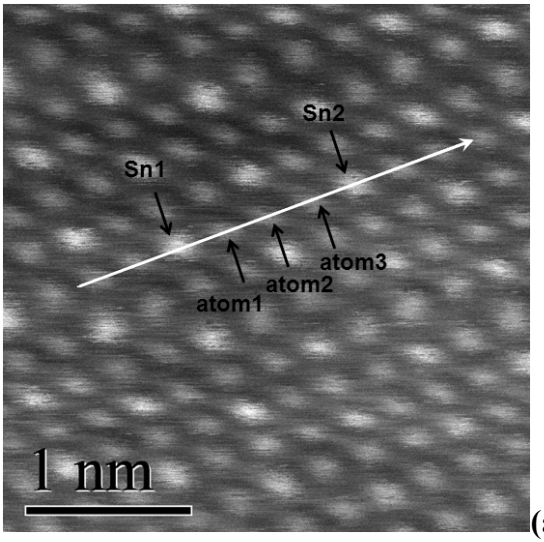

(a)

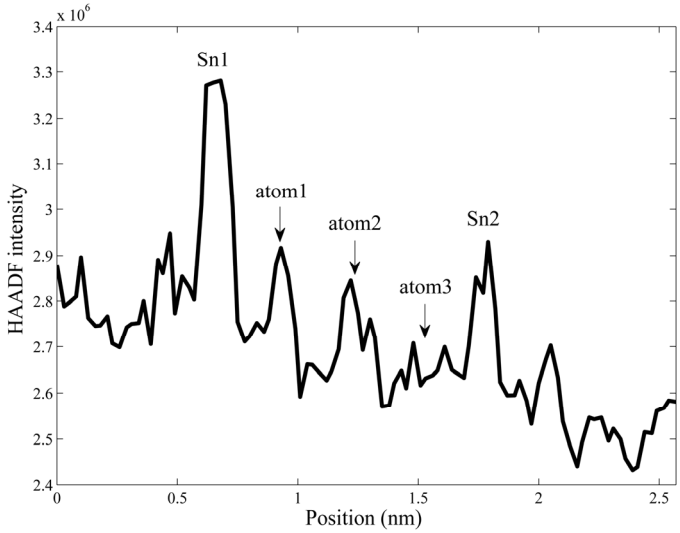

(b)

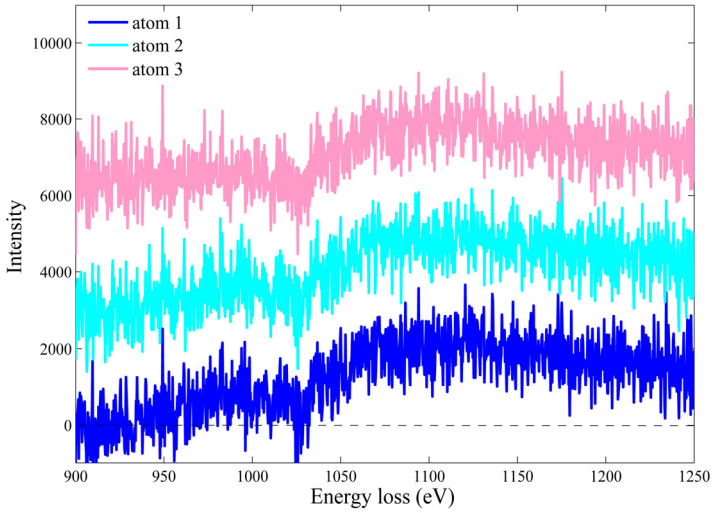

(c)

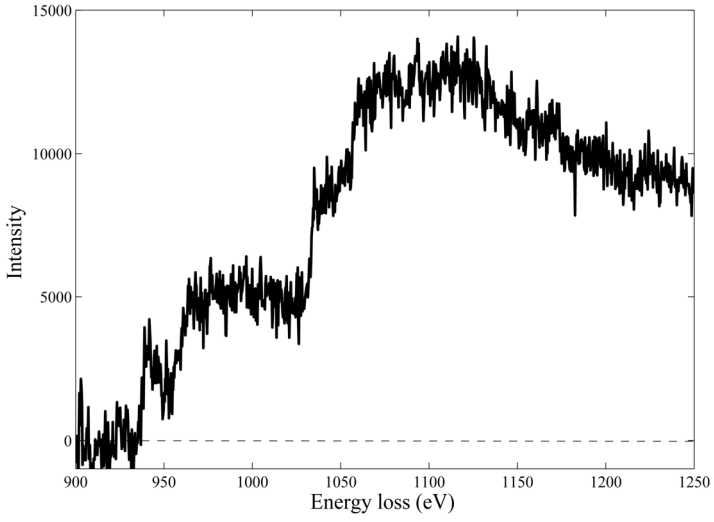

(d)

Figure 6. a) HAADF image of [010]-oriented CZTS. The arrow indicates the direction and line over which EELS spectra are acquired. The atom columns of interest are labeled Sn1, atom1, atom2, atom3 and Sn2 with the first and last being Sn atom columns. b) HAADF

intensity profile acquired simultaneously during EELS measurement. c) Extracted EELS spectra for atom columns atom1, atom2 and atom3 with the last two spectra vertically shifted for clarity. d) Average EELS spectrum over a 10x10 nm area acquired by rapidly scanning the electron beam over the area of interest during prolonged (i.e. 30 s) collection of the EELS spectrum. The area contained the atom columns of interest in Figure 6a.

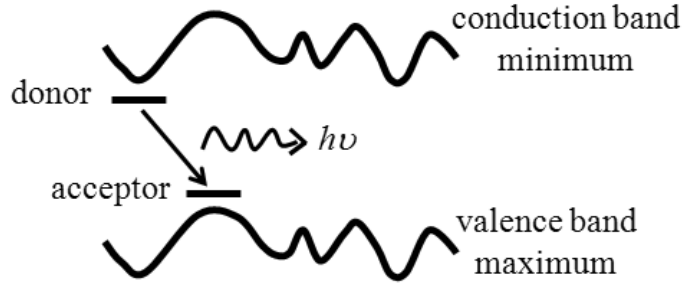

Figure 7: Schematic of the electronic band structure in CZTS. The conduction and valence band bending is due to a spatially fluctuating electrostatic potential. This causes broadening of the donor acceptor pair (DAP) peak in photoluminescence spectroscopy, since an electronic transition between spatially separated donor and acceptor levels emits radiation at a wavelength that is potentially different to that of a flat electronic band structure, the difference being a function of band bending at the donor and acceptor sites.

Table 1. Predicted bright field (BF) and whole pattern (WP) symmetry in CBED patterns for kesterite (KS) and stannite (ST) crystal structures in the <100> and <110> orientations. 'Full symmetry' and 'projection symmetry' refer to the situations where scattering from higher order Laue zones are strong and weak respectively.

Specimen and orientation	**Full symmetry**		**Projection symmetry**	
	BF	**WP**	**BF**	**WP**
KS <100>	*m*	1	2*mm*	*m*
ST <100>	2*mm*	2	2*mm*	2*mm*
KS <110>	*m*	1	2*mm*	*m*
ST <110>	2*mm*	*m*	2*mm*	*m*